

# Photon-starved imaging through turbulence at the diffraction limit

SEUNGMAN CHOI,<sup>1</sup> PETER MENART,<sup>1</sup> ANDREW SCHRAMKA,<sup>1</sup>  
 SHUBHANKAR JAPE,<sup>1</sup> LEIF BAUER,<sup>1</sup> IN-YONG PARK,<sup>2</sup> AND ZUBIN  
 JACOB<sup>1,\*</sup>

<sup>1</sup>*Elmore Family School of Electrical and Computer Engineering, Birck Nanotechnology Center, Purdue University, West Lafayette, Indiana 47907, USA.*

<sup>2</sup>*Emerging Research Instruments Group, Strategic Technology Research Institute, Korea Research Institute of Standards and Science (KRISS), 267 Gajeong-ro, Yuseong-gu, Daejeon 34113, South Korea*

<sup>\*</sup>[zjacob@purdue.edu](mailto:zjacob@purdue.edu)

**Abstract:** Ground-based imaging systems struggle to achieve diffraction-limited resolution when atmospheric turbulence and photon scarcity act simultaneously. In this regime, conventional adaptive optics, speckle imaging, and blind deconvolution lack sufficient information diversity to reliably estimate either the scene or the turbulence. We present Turbulence Aware Poisson Blind Deconvolution (TAP-BD), a framework designed for robust image recovery in these extreme conditions. TAP-BD extracts more information from coded-detection through phase diversity and decodes it with a physics-informed optimization that incorporates low photon Poisson statistics. Experiments show that TAP-BD provides reliable reconstructions of both scene and turbulence using only a few tens of measurements, even under strong aberrations and photon-starved conditions where existing methods fail. This capability enables photon-efficient, turbulence resilient imaging for applications such as space situational awareness and long-range remote sensing.

## 1. Introduction

Ground-based optical observations play a critical role in a wide range of applications, including space situational awareness [1, 2], exoplanet detection [3–5] and remote sensing [6]. A primary obstacle is atmospheric turbulence, which introduces time-varying wavefront distortions that blur the image and degrade resolution. To approach a telescope’s theoretical diffraction limit, these turbulence-induced aberrations must be estimated or corrected [7, 8]. In practice, turbulence evolves rapidly. Short exposure times are therefore used to “freeze” the wavefront dynamics [9]. While this reduces motion blur, it also limits the number of detected photons in each frame, resulting in noisy, low-signal measurements—especially for faint or distant targets [10]. Together, strong turbulence and limited photon counts place imaging systems in an information-starved regime. In this regime, both the object and the turbulence must be inferred from sparse and noisy measurements, a challenge that often exceeds the capabilities of conventional imaging and reconstruction approaches.

Existing strategies for imaging through turbulence, such as adaptive optics (AO), wavefront shaping (WS), and speckle imaging, are generally designed for scenarios with strong signal levels and a large number of measurements. AO systems employ dedicated wavefront sensors and deformable mirrors (DMs) to correct wavefront distortions. However, their reliance on bright guide stars and coarsely sampled wavefront limits their effectiveness in photon-starved conditions or severe aberration [11, 12]. WS can address higher-order aberration with fine spatial light modulator (SLM) control [13–17]. Despite this precision, this method still depends on strong calibration signals, making it less suitable for imaging faint, extended objects. Purely computational approaches offer an alternative by eliminating the need for a bright guide star. Among these, speckle imaging reconstructs a high-resolution image by analyzing statistical correlations within a series of short exposure speckle frames [18–20]. The primary trade-off,

however, is a substantial data requirement, often necessitating the collection of hundreds to thousands of frames to achieve a sufficient imaging performance. Another prominent method, blind deconvolution, seeks to jointly estimate the object and the aberration from the captured images [21–24]. Blind deconvolution models each measurement as the convolution of an unknown object with an unknown point spread function (PSF), and alternates between updating these two variables so that they consistently explain the captured data. Even in conventional settings, this inverse problem is highly ill-posed and thus typically restricted to simple blur models such as defocus or mild motion blur [25–27]. In astronomical and long-range imaging, however, atmospheric turbulence produces a far more complex and spatially varying PSF than those encountered in standard deconvolution problems, substantially increasing the difficulty of estimation [28, 29]. As a result, blind deconvolution has had limited practical use in astronomical imaging, and its performance in extremely low photon regimes remains largely unexplored.

We introduce turbulence-aware Poisson blind deconvolution (TAP-BD), a hardware-software co-design framework for imaging in turbulent, photon-starved conditions where conventional imaging methods become unreliable. Our approach begins with optical encoding, where an SLM applies a sequence of known phase patterns to the incoming wavefront. This process enriches and diversifies the information content of the measurements, such that each frame encodes complementary constraints on both the object and the turbulence, providing stronger cues for reconstruction. Because these encoded measurements are often dominated by shot noise in photon-starved regimes, TAP-BD first applies a dedicated Poisson denoiser [30]. This step suppresses shot noise while preserving the structural features essential for accurate estimation. The denoised measurements are then decoded computationally using a physics-informed optimization algorithm. It solves the joint estimation of the object and turbulence by decomposing the complex optimization into two tractable sub-problems. Each sub-problem admits efficient closed-form or proximal updates within an alternating-direction framework, ensuring stable optimization. Through simulations and experiments, we demonstrate that TAP-BD reliably achieves high-fidelity image reconstruction in information-starved regimes, offering a robust solution where conventional methods like AO and speckle imaging often fail.

## 2. Results

We begin by describing the TAP-BD hardware design which extracts additional information from the measurements to enhance reconstruction fidelity and resolution (Fig. 1). Faint light from the incoherent target  $O$  propagates through the turbulent medium and acquires an unknown phase distortion  $\Phi$ . At the system’s pupil, the SLM imposes a sequence of known phase patterns  $\{\Gamma_i\}_{i=1}^M$ , where  $M$  denotes the number of coded measurements. Each SLM phase pattern is generated by combining the first 15 Zernike polynomials with random coefficients, introducing controlled phase diversity across measurements. This phase diversity creates a set of uniquely coded intensity images  $\{I_i\}$  at the sensor plane. These measurements  $\{I_i\}$  are spatially distributed over detector pixels and weakly correlated both across pixels and across measurements due to the applied phase diversity  $\{\Gamma_i\}$ . This enriches and diversifies the information content of the data, resulting in a better-conditioned system for stable optimization [31].

Experimentally, this configuration is implemented using a 4f relay system. The first Fourier-transforming lens maps the object field to the pupil plane, where the SLM superposes the unknown turbulence phase  $\Phi$  with each known phase diversity pattern  $\Gamma_i$ . A second imaging lens then converts the modulated pupil field back to the image plane, forming intensity images of the target convolved with PSFs jointly determined by the turbulence  $\Phi$  and the SLM phase diversity  $\{\Gamma_i\}$ .

Fig. 1B shows the TAP-BD reconstruction pipeline, which estimates both the object and the turbulence phase from the optically encoded measurements. As a first step, we apply a plug-and-play (PnP) Poisson denoiser [30] to raw measurements  $\{I_i\}$  to mitigate shot noise.

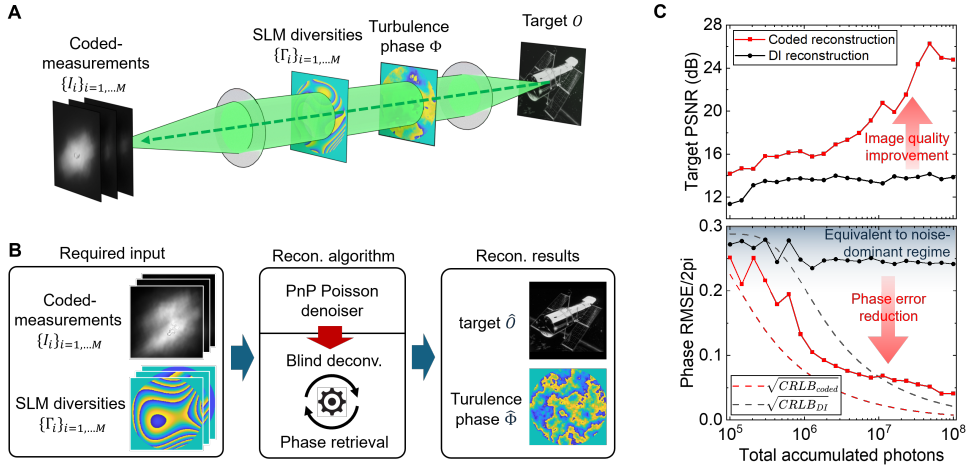


Fig. 1. Turbulence-Aware Poisson blind deconvolution (TAP-BD) framework. (A) Hardware setup: A spatial light modulator (SLM) sequentially imposes phase diversity patterns  $\{\Gamma_i\}$  on the incoming distorted wavefront, generating multiple coded-measurements  $\{I_i\}$ . (B) TAP-BD reconstruction pipeline: Each measurement is first denoised via a Poisson denoiser. An iterative solver then jointly recovers the target  $O$  and turbulence phase  $\Phi$  by leveraging both the denoised intensities  $\{P_i\}$  and the known SLM patterns  $\{\Gamma_i\}$ . (C) Plots show target PSNR (top) and phase RMSE (bottom) after reconstruction for the coded (red) versus DI (black). Cramer-Rao lower bounds (CRLBs) are also plotted for phase RMSE (dashed). The lower CRLB for the coded detection reflects higher information content. TAP-BD achieves better performance than DI by leveraging this additional information.

The PnP denoiser was originally developed as a standalone denoising method, but here we use it as a preprocessing stage to stabilize the subsequent reconstruction. This step is particularly important because blind deconvolution updates are highly sensitive to signal-dependent intensity fluctuations induced by Poisson shot noise, which can otherwise lead to unstable or degenerate solutions. The denoiser applies an Anscombe-wavelet transform to convert the Poisson noise into approximately Gaussian noise, followed by total variation (TV) smoothing to suppress measurement noise while preserving key structural details. An inverse transform then produces the denoised measurements  $\{P_i\}$ . When photons are sufficiently high, this denoising step is unnecessary and we directly set  $\{P_i\} = \{I_i\}$ . More details are available in the supplementary material.

With the denoised measurements  $\{P_i\}$ , the core task is to jointly estimate the object  $O$  and turbulence phase  $\Phi$ . We use three standard assumptions for image formation; static turbulence during acquisition, monochromatic/isoplanatic imaging, and phase-only turbulence distortions (See Appendix). Under these assumptions, the problem can be formulated as a single global loss:

$$L(O, \Phi) = \sum_{i=1}^M \frac{1}{2} \|O * |\mathcal{F}_i \Phi|^2 - P_i\|^2 \quad (1)$$

Where  $*$  denotes a convolution and  $\mathcal{F}_i$  is propagation operator for the  $i$ -th phase diversity  $\Gamma_i$ . We use angular spectrum method for  $\mathcal{F}_i$ , the detail of which can be found in the Appendix. The relationship between the turbulence  $\Phi$  and the final image  $\{P_i\}$  is highly indirect, due to wave propagation through  $\mathcal{F}_i$  followed by convolution  $*$ . This results in a severely ill-conditioned optimization landscape, making direct optimization of Eq. 1 unreliable.

Our key strategy is to split this complex problem into two simpler, physically-aligned sub-problems—blind deconvolution and phase retrieval—solved iteratively within the alternating direction method of multipliers (ADMM) frameworks. This separation yields stable closed-form updates for the object  $O$ , a set of PSFs  $\{h_i\}$ , and the turbulence phase  $\Phi$ , leveraging an alternating optimization structure commonly used in coded-imaging inverse problems [31]. Decoupling the loss into variable-specific sub-problems renders each update quadratic, enabling efficient and exact optimization.

First, the blind deconvolution block uses the measurements  $\{P_i\}$  to estimate the object  $O$  and an intermediate set of PSFs  $\{h_i\}$  by minimizing the constrained sub-problem defined by  $L_1$ :

$$L_1(O, h_i, T_O) = \sum_{i=1}^M \frac{1}{2} \|O * h_i - P_i\|^2 + \lambda \|\Psi O\|_1, \quad T_O = \Psi O \quad (2)$$

Here,  $\Psi$  denotes the TV operator,  $T_O$  is the corresponding auxiliary variable, and  $\lambda$  is the regularization weight. Although Poisson denoising already smooths the measurements, the TV term here further improves robustness to residual noise and regularizes the inverse problem, leading to more stable convergence. After reformulating it using an augmented Lagrangian, the resulting unconstrained sub-problem is quadratic in the variables  $O$ ,  $\{h_i\}$  and  $T_O$  in the Fourier domain, where the convolution reduces to pointwise multiplication. This structure enables the derivation of closed-form update rules for  $O$ ,  $\{h_i\}$  and  $T_O$ . Additional details are provided in the Supplementary Material.

Next, the wave-propagation block takes the provisional PSFs  $\{h_i\}$  from the previous blind deconvolution block and finds for the underlying turbulence phase  $\Phi$  by minimizing sub-loss  $L_2$ :

$$L_2(\{u_i\}, \Phi) = \sum_{i=1}^M \frac{1}{2} \left\| \sqrt{h_i} - |\mathcal{F}_i \Phi| \right\|^2, \quad u_i = \mathcal{F}_i \Phi \quad (3)$$

Here,  $u_i$  denotes the auxiliary efield corresponding to the  $i$ -th PSF at the detector plane. This sub-problem is also proximally quadratic in the variables  $\Phi$  and  $\{u_i\}$  in the Fourier domain, where the wave propagation operator  $\mathcal{F}_i$  reduces to pointwise multiplication. This structure enables closed-form update rules for both the PSFs  $\{h_i\}$  and the turbulence phase  $\Phi$ . After updating the turbulence phase  $\Phi$ , a physically consistent set of PSFs is recomputed as  $h_i = |\mathcal{F}_i \Phi|^2$ . These updated PSFs are then fixed and passed back to the blind deconvolution block, where they are used to re-estimate the object  $O$  in the next ADMM iteration. Through iterative alternating updates, TAP-BD enforces physical consistency between the convolution and wave propagation models via shared PSF variables. When combined with the information gain provided by phase-diverse coded detection, the TAP-BD framework enables robust estimation from a limited number of measurements under severe turbulence and low-photon conditions. Full derivations of the closed-form update rules are provided in the Supplementary Material.

A comparison between TAP-BD and direct imaging (DI), a baseline approach without phase diversity, highlights the role of phase diversity in enhancing information content and estimation accuracy (Fig. 1C). We evaluate two metrics: the peak signal-to-noise ratio (PSNR) of the target intensity and the root-mean-square error (RMSE) of the turbulence phase (see the Appendix for details). As photon levels decrease, both methods show overall performance degradation, with decreasing target PSNR and increasing phase RMSE. However, TAP-BD consistently outperforms DI, achieving higher PSNR and lower phase RMSE across all photon levels. This improvement partially comes from the additional information provided from phase diversity, which enables more efficient use of the limited photon budget. To quantify this, we plot the phase Cramer–Rao lower bound (CRLB). Notably, TAP-BD achieves a lower phase CRLB than DI, indicating that it extracts more information under identical photon constraints. Moreover, the achieved phase RMSE closely approaches this theoretical bound, highlighting that our TAP-BD algorithm is

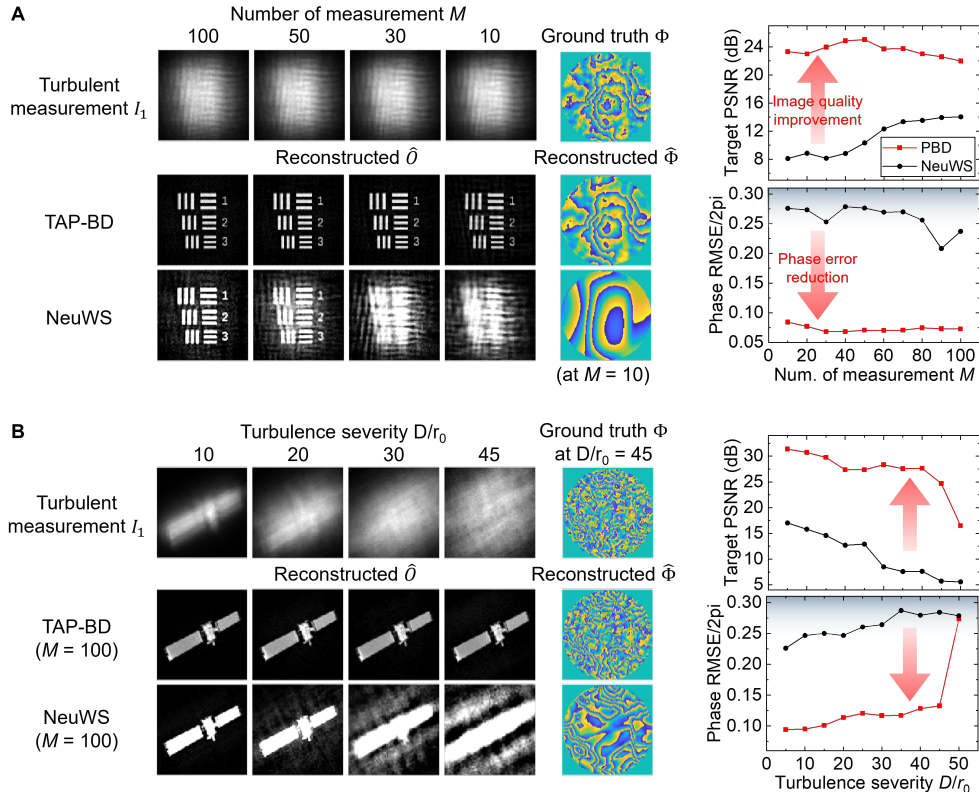


Fig. 2. Comparative simulation of TAP-BD and NeuWS: (A) varying measurement count  $M$  (at fixed turbulence strength  $D/r_0 = 20$  and total photon budget  $5 \times 10^8$ ) and (B) varying turbulence severity  $D/r_0$  (at fixed  $M = 100$  and total photon budget  $1 \times 10^9$ ). The left panels show turbulent only measurement  $I_1$  with flat phase diversity  $\Gamma_1$ , reconstructed targets  $\hat{O}$  and estimated turbulence phases  $\hat{\Phi}$  for each method. The right panels show corresponding target PSNR and phase RMSE. Note that we modified NeuWS to incorporate the assumption of uniform intensity across the circular pupil aperture to match with TAP-BD simulating phase-only distortion at the pupil plane. Both methods use 1000 iterations/epochs. Poisson denoiser was not used for TAP-BD in these simulations.

effectively designed to take advantage of the enhanced information gain given by coded hardware. These findings also align with prior wavefront randomization analysis [21], where WS improves spatial frequency response, thereby facilitating improved reconstruction in the deconvolution process. Further details on the CRLB calculations are provided in the Appendix.

Fig. 2 summarizes the simulation results that highlight the effectiveness of our TAP-BD's software approach in challenging conditions with limited measurements  $M$  and strong turbulence severity  $D/r_0$ . We compare TAP-BD with NeuWS [28], a noteworthy neural network benchmark which treats the set of measurements as training data and uses neural networks to model both the target and the aberrations. Note that both methods operate under the same coded detection hardware setup, allowing us to see the impact of different reconstruction strategies in such extreme conditions. The calculation of turbulence severity  $D/r_0$  can be found in the Appendix.

We first vary the number of measurements  $M$  at fixed turbulence strength  $D/r_0 = 20$  and a fixed photon budget  $N$  (Fig. 2A). Across all values of  $M$ , TAP-BD consistently achieves higher

Table 1. Execution time comparison between TAP-BD and NeuWS (each using 1000 iterations/epochs) on a standard GeForce RTX 3060Ti GPU.

Number of measurements ( $M$ )	TAP-BD (s)	NeuWS (s)
10	6.0	49
20	9.2	76
40	16.7	137
100	38.6	344

target PSNR and lower phase RMSE than NeuWS. NeuWS performs competitively when a large number of measurements is available (e.g.  $M = 100$ ); however, its performance degrades rapidly as  $M$  decreases. With only  $M = 10$ , TAP-BD attains  $\sim 24$  dB PSNR and a phase RMSE/ $2\pi$  of  $\sim 0.07$ , whereas NeuWS yields a noisier reconstruction with only  $\sim 8$  dB PSNR and a heavily smoothed phase reconstruction that misses complex features, leading to the much higher phase RMSE/ $2\pi$  of 0.27.

In Fig. 2B, we vary the turbulence severity  $D/r_0$  at fixed  $M = 100$ . TAP-BD remains robust up to  $D/r_0 \sim 45$ , achieving  $\sim 25$  dB PSNR and phase RMSE/ $2\pi$  of  $\sim 0.12$ . NeuWS degrades sharply under the same conditions, with  $\sim 8$  dB PSNR and RMSE/ $2\pi$  of  $\sim 0.27$ , often producing saturated or overly simplified reconstruction. These findings highlight TAP-BD’s superior efficiency in the information-starved regime. Neural network-based methods such as NeuWS rely on data availability to effectively constrain a highly expressive model, performing well when sufficient measurements are available but becoming unreliable as data become scarce. In such regimes, insufficient constraints lead to unstable optimization and convergence to degenerate solutions, such as binarized images or oversmoothed turbulence estimates. In contrast, TAP-BD explicitly constrains the inverse problem through a physics-based forward model and a low-dimensional set of physically meaningful variables. These explicit physical constraints reduce the dependence on large data volumes for regularization, enabling reliable reconstruction under severe turbulence and limited measurements. This result underscores that for such challenging problems, the algorithm design is as critical as the hardware itself.

In addition to improving reconstruction quality, TAP-BD achieves high computational efficiency. (Table 1). On an RTX 3060Ti GPU, NeuWS takes 344 s for  $M = 100$  measurements, whereas TAP-BD takes just 38.6 s—a 9× reduction in computational time. At  $D/r_0 = 20$  (Fig. 2A), TAP-BD reaches high-quality results with only  $M = 10$  measurements in  $\sim 6$  s, a 57× reduction compared with NeuWS at  $M = 100$ . This computational efficiency comes from updating few, physically meaningful variables and from closed-form or proximal updates built from 2D FFT only, giving per-update cost  $O(N \log(N))$ , with  $N = 256 \times 256$  in this analysis.

Next, we experimentally evaluated the robustness of TAP-BD across varying turbulence levels  $D/r_0$  in Fig. 3. For these experiments, we used a negative 1951 USAF target (R3L3S1N, Thorlabs) as the test object  $O$ . The ground-truth turbulence phase  $\Phi$  was generated and displayed on a SLM (E19×12-400-800-HDM8, 1920×1200 pixels with 8  $\mu\text{m}$  pixel pitch, Meadowlark Optics), where it was superposed with each of the phase diversity patterns  $\{\Gamma_i\}$ . The corresponding coded measurements  $\{I_i\}$  were sequentially captured using an emCCD camera (PIMAX 4:512EM, 512×512 pixels with 23.6  $\mu\text{m}$  pixel pitch, Teledyne Princeton Instruments). Details on the system configuration can be found in the Supplementary Material, while photon calculations are provided in the Appendix.

Fig. 3A demonstrates TAP-BD’s performance under turbulence level  $D/r_0 = 20$ . Notably, with as few as  $M = 12$  measurements, the reconstructed target  $\hat{O}$  achieves  $\sim 26$  dB PSNR,

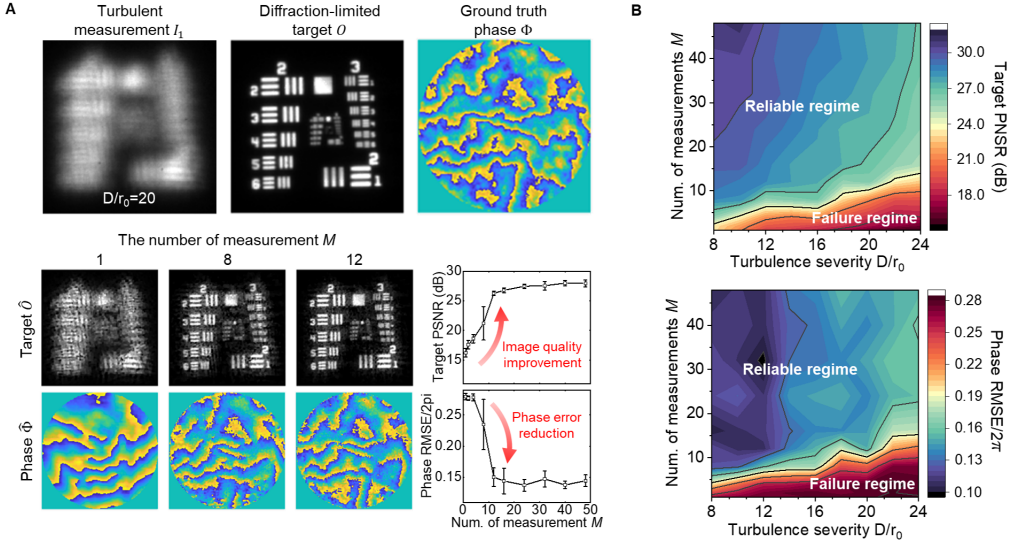


Fig. 3. Experimental reconstruction under varying turbulence severity level  $D/r_0$  and measurement count  $M$ , averaged over five distinct turbulence phases per  $D/r_0$ . (A) Example reconstruction results at  $D/r_0 = 20$ : The top panel shows the turbulent measurement  $I_1$  with flat phase diversity  $\Gamma_1$ , diffraction-limited image of the USAF 1951 target  $O$  and ground truth turbulence phase  $\Phi$ . The bottom plot illustrates how increasing  $M$  boosts reconstruction quality, as measured by target PSNR, and phase RMSE (bottom-right). (B) Contour plots of the target PSNR (top) and phase RMSE (bottom) as functions of  $D/r_0$  and  $M$ . All experiments were conducted with a high photon flux ( $\sim 2.13 \times 10^7$  photons per single measurement), using a 5 mm aperture and 1000 iterations per reconstruction. A Poisson denoiser was not employed.

and the estimated phase  $\hat{\Phi}$  attains an RMSE/2 $\pi$  of  $\sim 0.15$ . This high fidelity indicates that the reconstruction resolves fine spatial features approaching the system's diffraction-limited resolution, which corresponds to Group 3, Element 4 of the USAF target (11.31 line pairs/mm, or approximately 44  $\mu\text{m}$  resolution). These experimental results align with our simulations (Fig. 2A), which also indicated that  $M \sim 10$  measurements are sufficient for turbulence level of  $D/r_0 \sim 20$ .

The relationship between turbulence severity  $D/r_0$  and the number of measurements  $M$  required to maintain reconstruction quality is summarized in Fig. 3B. As expected, stronger turbulence generally demands more measurements to achieve a fixed level of fidelity, revealing an inherent measurement-turbulence trade-off. Importantly, TAP-BD shifts this trade-off toward substantially fewer measurements. Using a target PSNR of approximately 24 dB as a representative threshold for high-fidelity reconstruction, TAP-BD typically requires fewer than 15 measurements when  $D/r_0 \leq 24$ . This low-measurement regime is inaccessible to conventional blind deconvolution methods under comparable turbulence conditions [27]. As turbulence severity increases beyond this range, TAP-BD continues to deliver reliable reconstructions by moderately increasing  $M$ , as shown in Fig. 2B. Even in this regime, TAP-BD can operate with far fewer measurements than prior approaches [28], substantially expanding the feasible operating range of blind deconvolution under severe aberrations and limited data. This efficiency directly enables high-speed acquisition by minimizing the number of frames required per reconstruction.

Lastly, we evaluate TAP-BD in the photon-starved regime, where blind deconvolution becomes unstable due to strong, signal-dependent Poisson noise (Fig. 4). Such noise corrupts the measured

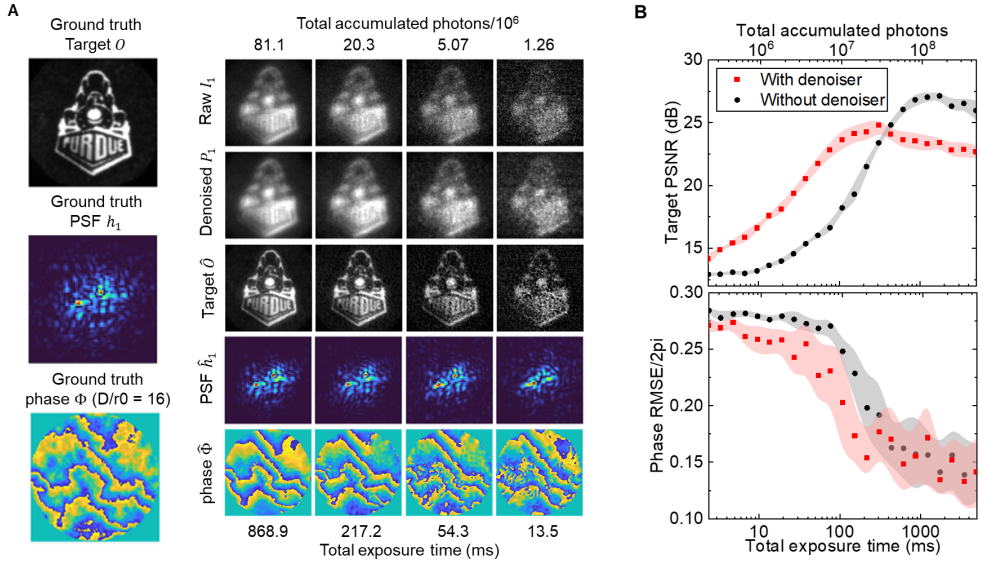


Fig. 4. Experimental reconstruction under low photon levels, averaged over five distinct turbulence phases at fixed  $D/r_0 = 16$ . (A) Example reconstructions. The left panel shows ground truth elements: the diffraction limited image of ‘Purdue train’ target  $O$ , the turbulent PSF  $h_1$  with flat phase diversity  $\Gamma_1$  and the turbulence phase  $\Phi$ . The right panels illustrate reconstruction results at different photon levels. The first row shows raw measurements  $I_1$ , highlighting how shot noise becomes dominant as photon count decreases. The second row presents Poisson-denoised measurements  $P_1$ . Rows three to five display the reconstructed target  $\hat{O}$ , estimated PSF  $\hat{h}_1$  and retrieved phase  $\hat{\Phi}$ . (B) Target PSNR and phase RMSE with and without Poisson denoising. In the low-photon regime, denoising significantly boosts PSNR and lowers phase RMSE. Shaded regions denote the  $\pm$  one standard deviation computed over five independent trials with different turbulence phases. All experiments used a 3 mm aperture,  $M = 48$  measurements, and 1000 iterations per reconstruction.

intensities and propagates into the estimation updates, severely degrading reconstruction accuracy at low photon counts. To address this challenge, TAP-BD incorporates a Poisson denoising step that stabilizes the measurements prior to reconstruction. We test this approach using a laser-printed “Purdue train” logo on transparent film (1200 dpi,  $\sim 0.0212$  mm dot spacing), with turbulence severity  $D/r_0 = 16$  and  $M = 48$  measurements. Fig. 4A shows that while the raw measurements  $I_1$  become increasingly noisy as photon levels decrease, the denoised measurements  $P_1$  preserve the underlying structure with substantially reduced noise. The subsequent rows display the reconstructed target  $\hat{O}$  turbulent PSF  $\hat{h}_1$ , and turbulence phase  $\hat{\Phi}$ . Despite the lower photon levels—and the accompanying inherent reduction in accuracy—the key structural features of the target, PSF and turbulence are well preserved.

Fig. 4B illustrates the role of the Poisson denoiser across different photon budgets and clarifies when its use is most beneficial. In the low-photon regime, applying the denoiser leads to a clear improvement in target PSNR (top panel), indicating more stable and accurate reconstruction under severe shot noise. As photon counts increase, smoothing regularization becomes less necessary, and the denoiser provides diminishing benefit, suggesting that its use should be adapted to the photon flux. Importantly, the denoiser also yields a meaningful reduction in phase RMSE in the low photon regime (bottom panel). Its benefit becomes more evident in optical

correction experiments (see Supplementary Materials), where reconstruction quality is assessed through physical correction performance through the estimated turbulence phase. Incorporating denoising leads to substantially improved optical correction, indicating that denoising preserves the essential wavefront structure required for effective turbulence compensation. In contrast, without denoising, shot noise contaminates both the object and phase updates, producing highly fluctuating, unphysical estimates that cause optical correction to break down entirely. These results highlight a key practical implication of the Poisson denoiser. By stabilizing shot noise-dominated measurements, it enables reliable reconstruction of faint targets under short-exposure conditions required for rapidly varying turbulence. This stabilization allows TAP-BD to remain effective in regimes where low photon flux and fast turbulence dynamics would otherwise severely degrade imaging performance.

### 3. Discussion

TAP-BD currently adopts three standard simplifying assumptions: static turbulence during acquisition, isoplanatic aberrations, and monochromatic illumination. Temporal stationarity requires measurements to be acquired faster than the turbulence evolution, which can be addressed through higher-speed SLMs [32–34] and cameras or by explicitly modeling temporal correlations across sequential acquisitions [35]. The isoplanatic assumption restricts the field of view to the memory-effect region, but can be relaxed using spatially varying or multiplanar forward models to accommodate anisoplanatic aberrations [36–38]. Finally, while the current implementation assumes monochromatic illumination, extensions to broadband or multispectral imaging are feasible by incorporating partial temporal coherence or spectral channelization [39].

In conclusion, we have shown that TAP-BD can estimate the target and turbulence phase with high accuracy in the information-starved regime with few measurements, strong turbulence and low-photon conditions. The algorithm recovers the turbulence phase with errors approaching theoretical limits and achieves compelling target reconstruction fidelity. Notably, TAP-BD attains  $\sim 24$  dB target PSNR up to  $D/r_0 \sim 24$  with only ten measurements, and performance in photon-starved regimes improves further with Poisson denoising. These results enable photon-limited, fast imaging in long-range, turbulence-distorted settings. This is important for various applications, such as ground-based space situational awareness, exoplanet detection, and remote sensing.

### Appendix A: Target PSNR and phase RMSE calculation

Our TAP-BD algorithm is inherently unable to correct for tip-tilt errors. This limitation arises because an infinite number of tip-tilt phase and target position combinations can yield the same measurement, making it impossible to uniquely determine the true tip-tilt component. Consequently, to compute the PSNR and phase RMSE, we introduce the assumption that the ground target  $O$  position is known. Specifically, for the target PSNR calculation, we first determine the lateral shift between the reconstructed target  $\hat{O}$  and the ground truth  $O$  by computing their cross-correlation:

$$C(\Delta x, \Delta y) = \sum_{x,y} O(x, y) \hat{O}(x + \Delta x, y + \Delta y) \quad (\text{A1})$$

where  $(x, y)$  is detector pixel coordinate.

The optimal shift  $(\Delta x^*, \Delta y^*)$  corresponding to the peak of the correlation is then given by:

$$(\Delta x^*, \Delta y^*) = \text{argmax}[C(\Delta x, \Delta y)] \quad (\text{A2})$$

Using this shift, we align the reconstructed target:  $\hat{O}^*(x, y) = \hat{O}(x + \Delta x^*, y + \Delta y^*)$ , which

allows us to compute the target PSNR:

$$\text{PSNR} = 10 \log_{10} \left( \frac{\max(O)^2}{\frac{1}{K} \sum_{x,y} [O(x,y) - \hat{O}^*(x,y)]^2} \right), \quad (\text{A3})$$

where  $K$  is the total number of target pixels.

Furthermore, the obtained lateral shift is converted into an equivalent tip/tilt phase correction. For example, assuming a linear phase ramp, the tip/tilt correction can be expressed as:

$$\Delta(x, y) = \frac{2\pi}{\lambda} \frac{s}{f} (\Delta x^* x + \Delta y^* y), \quad (\text{A4})$$

where  $\lambda$  is the wavelength,  $s$  is detector pixel size, and  $f$  is focal length of imaging lens.

The reconstructed phase  $\hat{\Phi}$  is then corrected by adding the tip/tilt components:  $\hat{\Phi}^*(x, y) = \hat{\Phi}(x, y) \exp(j \Delta(x, y))$ .

Because phase is inherently cyclic, the standard RMSE does not properly account for phase wrapping and may yield different errors for different global phase shifts—even though a global phase shift is not physically meaningful. To address this issue, we define the absolute phase error between two angles  $\angle\Phi$  and  $\angle\hat{\Phi}^*$  as:

$$E(\Phi, \hat{\Phi}^*) = \begin{cases} |\angle\Phi - \angle\hat{\Phi}^*|, & \text{if } |\angle\Phi - \angle\hat{\Phi}^*| \leq \pi, \\ 2\pi - |\angle\Phi - \angle\hat{\Phi}^*|, & \text{otherwise.} \end{cases} \quad (\text{A5})$$

The phase RMSE is then calculated as:

$$\text{RMSE} = \sqrt{\frac{1}{K} \sum_{x,y} [E(\Phi, \hat{\Phi}^*)]^2}, \quad (\text{A6})$$

where  $K$  is total number of phase pixels. This metric is invariant to global phase offset.

## Appendix B: Assumption for image modeling

We make several assumptions to enable robust modeling and reconstruction as follows.

First, we assume the turbulence  $\Phi$  remains constant throughout all  $M$  measurements. This assumption holds when the entire data acquisition process occurs within the turbulence correlation time, ensuring all measurements share the same turbulence phase.

Second, we adopt a monochromatic and isoplanatic imaging model. Under the isoplanatic assumption, the PSF remains shift-invariant across the field of view due to the optical memory effect [40], allowing us to assign a single PSF per measurement.

Finally, we assume negligible amplitude variations at the pupil plane, allowing us to model the pupil field with a flat amplitude and a phase term composed of the unknown turbulence  $\Phi$  and known SLM pattern  $\Gamma_i$ . This assumption is valid in long-range imaging scenarios, such as astronomical observation, where most turbulence occurs far from the target and near the telescope, leading to primarily phase-only distortions.

## Appendix C: Kolmogorov turbulence theory

Kolmogorov turbulence theory provides a realistic approach for simulating atmospheric turbulence, particularly when rapid turbulence variations make the Zernike-based approximation unsuitable. To generate a single turbulence phase map  $\Phi(\mathbf{x})$ , where  $\mathbf{x} = (x, y)$ , we define the turbulence severity  $D/r_0$ , with  $D$  as the aperture diameter at the pupil-plane and  $r_0$  as the Fried parameter representing the maximum distance for coherent light transmission through the turbulence:

$$r_0 = \left( 0.423k^2 \int_L C_n^2(z) dz \right)^{-3/5} \quad (C1)$$

where  $k$  is the optical wavenumber and  $C_n^2$  is the refractive index structure constant over the propagation path  $L$ .

The power spectral density (PSD)  $P(\mathbf{k})$ , describing phase fluctuations across spatial frequencies  $\mathbf{k} = (k_x, k_y)$ , follows Kolmogorov's model:

$$P(\mathbf{k}) = 0.4961 r_0^{-5/3} \mathbf{k}^{-11/3} \quad (C2)$$

We define the complex turbulence spectrum with random phase distribution:

$$S_{\text{turb}}(\mathbf{k}) = \sqrt{P(\mathbf{k})} \eta(\mathbf{k}) \quad (C3)$$

where  $\eta(\mathbf{k})$  is complex Gaussian noise with zero mean and standard deviation  $\sigma = 1$ .

The turbulence phase map  $\Phi(\mathbf{x})$  is obtained via the inverse Fourier transform:

$$\Phi(\mathbf{x}) = \mathbf{F}^{-1}[S_{\text{turb}}(\mathbf{k})] \quad (C4)$$

This phase screen  $\Phi(\mathbf{x})$  simulates the effect of random turbulence over  $L$  for a specific  $r_0$ .

## Appendix D: Wave propagator

To simulate the e-field propagation over a distance  $z$ , we use an angular spectrum method (ASM), denoted as  $A_z$ . The ASM operator is defined as:

$$e_{\text{out}}(x, y) = \mathcal{A}_z e_{\text{in}}(x, y) = \mathbf{F}^{-1}[\mathbf{H}(k_x, k_y, z) \cdot \mathbf{F}[e_{\text{in}}(x, y)]] \quad (D1)$$

where  $e_{\text{in}}(x, y)$  is the input e-field,  $e_{\text{out}}(x, y)$  is the propagated field, and  $\mathbf{F}$  and  $\mathbf{F}^{-1}$  represent the Fourier and inverse Fourier transform, respectively.

The transfer function  $\mathbf{H}(k_x, k_y, z)$  for distance  $z$  is:

$$\mathbf{H}(k_x, k_y, z) = \exp\left(\frac{2j\pi z}{\lambda} \sqrt{1 - \lambda^2(k_x^2 + k_y^2)}\right) \quad (D2)$$

Here,  $k_x$  and  $k_y$  are spatial frequency components, and  $\lambda$  is the wavelength. Above expression holds if  $k_x^2 + k_y^2 \leq 1$ , and is 0 otherwise.

For simulating field propagation between sequential optical elements, such as from the SLM to an imaging lens, and from the lens to a detector, we use:

$$u_i = \mathcal{F}_f(\Phi) = \mathcal{A}_f \{ \mathcal{A}_f [A \cdot \Phi \cdot \Gamma_i] \cdot R \} \quad (D3)$$

where  $u_i$  is the resulting image plane e-field,  $\Phi$  is the pupil plane turbulence e-field (the target field to retrieve),  $A$  is the aperture constraint,  $\Gamma_i$  is the  $i$ -th phase diversity pattern applied by the SLM, and  $R$  is the imaging lens phase with focal length  $f$ .

## Appendix E: CRLB calculation

To explain the theoretical phase accuracy limit shown in Fig. 1C of the main text, we computed the Fisher information and derived the corresponding Cramér-Rao Lower Bound (CRLB). Fisher information quantifies how much information measurements contain about unknown parameters.

In this analysis, the full parameter vector is defined as  $\Theta = \{\{\Phi_a\}_{a=1}^A, \{O_b\}_{b=1}^B\}$ , where the phase parameters have  $A = 1184$  (the effective number of phase pixels within a circular aperture of 40 pixels in diameter) and the target intensity parameters have  $B = 1600$  (corresponding to a

$40 \times 40$  image). Here, we focus solely on phase accuracy. In this simulation, we acquire  $M = 10$  different coded measurements across  $K$  detector pixels.

The Fisher information matrix (FIM) is then defined by:

$$J_{pq} = \sum_{k=1}^K \sum_{i=1}^M \frac{1}{\mu_{ik}} \left( \frac{\partial \mu_{ik}}{\partial \Phi_p} \right) \left( \frac{\partial \mu_{ik}}{\partial \Phi_q} \right), \quad (\text{E1})$$

where  $\mu_{ik}$  is the mean single-photon intensity at detector pixel  $k$  for the  $i$ -th coded-detection measurement.

Since the measurements are invariant to a global phase shift (the piston effect), the FIM is singular. To resolve this ambiguity, we fix the phase at one pixel—removing the corresponding row and column from the FIM following [41]—and then invert the resulting dimension-reduced FIM to obtain the CRLB matrix  $\sigma^2$ .

The diagonal elements of the CRLB matrix  $\sigma^2$  represent the minimum variance achievable by any unbiased estimator for each parameter. Therefore, we calculate the mean standard deviation  $\bar{\sigma}$  of phase as:

$$\bar{\sigma}(N) = \sqrt{\frac{1}{N(A-1)} \sum_{a=1}^{A-1} \sigma_{aa}^2}, \quad (\text{E2})$$

where  $N$  is the photon count. This metric represents the theoretical limit of phase accuracy at a given photon level  $N$  for the coded measurements.

## Appendix F: Photon number measurement

We calculate the photon count using two methods. The first method is based on the EM-CCD measurement, where the photon count  $N_{\text{EM}}$  is computed from the intensity image  $I(x)$  as:

$$N_{\text{EM}} = \sum_x \frac{I(x)}{Q_{\text{EM}} \cdot G} \quad (\text{F1})$$

where  $Q_{\text{EM}}$  is the quantum efficiency of the EM-CCD, and  $G$  is the system gain.

The second method uses a photodiode (S120VC, Thorlabs) to obtain a reference photon counts  $N_{\text{PM}}$ :

$$N_{\text{PM}} = P \cdot \frac{\lambda}{hc} \cdot \frac{1}{Q_{\text{PM}}} \quad (\text{F2})$$

where  $P$  is the measured power,  $hc/\lambda$  is the energy per photon, and  $Q_{\text{PM}}$  is the quantum efficiency of the photodiode.

Upon comparing  $N_{\text{PM}}$  and  $N_{\text{EM}}$ , we found that  $N_{\text{PM}}$  was about 20% higher than  $N_{\text{EM}}$  at low photon levels. Because the power meter method provides a more direct measurement, we use it as a reference, adjusting the EM-CCD-derived photon counts as  $1.2N_{\text{EM}}$ .

**Funding.** This work was supported by the Air Force Office of Scientific Research (AFOSR, grant FA9550-24-1-0345) and the Technology Innovation Program (IRIS no. RS-2024-00419426) funded by the Ministry of Trade, Industry and Energy (MOTIE, Korea).

**Disclosures.** The authors declare no conflicts of interest.

**Data Availability.** All data needed to evaluate the conclusions in the paper are present in the paper and/or the Supplementary Materials.

**Supplemental document.** See Supplement 1 for supporting content.

## References

1. J. R. Shell, "Optimizing orbital debris monitoring with optical telescopes," Schriever Air Force Base TR ADA531931 (2010).
2. H. Choi, S. Choi, P. Menart, *et al.*, "Telescope imaging beyond the rayleigh limit in extremely low snr," *New J. Phys.* **26**, 093019 (2024).
3. J.-F. Sauvage, L. M. Mugnier, G. Rousset, and T. Fusco, "Analytical expression of long-exposure adaptive-optics-corrected coronagraphic image. first application to exoplanet detection," *J. Opt. Soc. Am. A* **27**, A157–A170 (2010).
4. S. Choi, P. Menart, A. Schramka, *et al.*, "Poisson wavefront imaging in photon-starved scenarios," *Opt. Open* (2025). Preprint. <https://doi.org/10.1364/opticaopen.30223318.v1>.
5. F. Bao, H. Choi, V. Aggarwal, and Z. Jacob, "Quantum-accelerated imaging of n stars," *Opt. Lett.* **46**, 3045–3048 (2021).
6. J.-P. Lagourde, M. Irvine, and S. Dupont, "Atmospheric turbulence induced errors on measurements of surface temperature from space," *Remote. Sens. Environ.* **168**, 40–53 (2015).
7. Z. Mao, N. Chmitt, and S. H. Chan, "Image reconstruction of static and dynamic scenes through anisoplanatic turbulence," *IEEE Trans. on Comput. Imaging* **6**, 1415–1428 (2020).
8. S. H. Chan, N. Chmitt *et al.*, "Computational imaging through atmospheric turbulence," *Found. Trends Comput. Graph. Vis.* **15**, 253–508 (2023).
9. R. G. Paxman, T. J. Rogne, B. A. Sickmiller, *et al.*, "Spatial stabilization of deep-turbulence-induced anisoplanatic blur," *Opt. Express* **24**, 29109–29125 (2016).
10. R.-y. Sun, J.-w. Zhan, C.-y. Zhao, and X.-x. Zhang, "Algorithms and applications for detecting faint space debris in geo," *Acta Astronaut.* **110**, 9–17 (2015).
11. B. R. Norris, J. Wei, C. H. Betters, *et al.*, "An all-photonic focal-plane wavefront sensor," *Nat. Commun.* **11**, 5335 (2020).
12. G.-H. Go, D.-g. Lee, J. Oh, *et al.*, "Meta shack–hartmann wavefront sensor with large sampling density and large angular field of view: phase imaging of complex objects," *Light. Sci. & Appl.* **13**, 187 (2024).
13. E. J. Candès, X. Li, and M. Soltanolkotabi, "Phase retrieval from coded diffraction patterns," *Appl. Comput. Harmon. Anal.* **39**, 277–299 (2015).
14. Y. Wu, M. K. Sharma, and A. Veeraraghavan, "Wish: wavefront imaging sensor with high resolution," *Light. Sci. & Appl.* **8**, 44 (2019).
15. P. Lai, L. Wang, J. W. Tay, and L. V. Wang, "Photoacoustically guided wavefront shaping for enhanced optical focusing in scattering media," *Nat. photonics* **9**, 126–132 (2015).
16. R. Horstmeyer, H. Ruan, and C. Yang, "Guidestar-assisted wavefront-shaping methods for focusing light into biological tissue," *Nat. photonics* **9**, 563–571 (2015).
17. A. P. Mosk, A. Lagendijk, G. Lerosey, and M. Fink, "Controlling waves in space and time for imaging and focusing in complex media," *Nat. photonics* **6**, 283–292 (2012).
18. O. Katz, P. Heidmann, M. Fink, and S. Gigan, "Non-invasive single-shot imaging through scattering layers and around corners via speckle correlations," *Nat. photonics* **8**, 784–790 (2014).
19. W.-Y. Chen, M. O'Toole, A. C. Sankaranarayanan, and A. Levin, "Enhancing speckle statistics for imaging inside scattering media," *Optica* **9**, 1408–1416 (2022).
20. S. Sun, Z.-W. Nie, L.-K. Du, *et al.*, "Overcoming the diffraction limit by exploiting unmeasured scattering media," *Optica* **11**, 385–391 (2024).
21. A. Kohli, A. N. Angelopoulos, and L. Waller, "Wavefront randomization improves deconvolution," in *Computational Optical Imaging and Artificial Intelligence in Biomedical Sciences*, vol. 12857 (SPIE, 2024), pp. 27–38.
22. C. S. Huebner and M. Greco, "Blind deconvolution algorithms for the restoration of atmospherically degraded imagery: a comparative analysis," in *Optics in Atmospheric Propagation and Adaptive Systems XI*, vol. 7108 (SPIE, 2008), pp. 166–177.
23. X. Zhu and P. Milanfar, "Removing atmospheric turbulence via space-invariant deconvolution," *IEEE transactions on pattern analysis machine intelligence* **35**, 157–170 (2012).
24. S. Guo, Y. Lu, and Y. Li, "Richardson–lucy iterative blind deconvolution with gaussian total variation constraints for space extended object images," in *Photonics*, vol. 11 (MDPI, 2024), p. 576.
25. Y. Sanghvi, A. Gnanasambandam, Z. Mao, and S. H. Chan, "Photon-limited blind deconvolution using unsupervised iterative kernel estimation," *IEEE Trans. on Comput. Imaging* **8**, 1051–1062 (2022).
26. V. Debarnot and P. Weiss, "Deep-blur: Blind identification and deblurring with convolutional neural networks," *Biol. Imaging* **4**, e13 (2024).
27. C. Johnson, M. Guo, M. C. Schneider, *et al.*, "Phase-diversity-based wavefront sensing for fluorescence microscopy," *Optica* **11**, 806–820 (2024).
28. B. Y. Feng, H. Guo, M. Xie, *et al.*, "Neuws: Neural wavefront shaping for guidestar-free imaging through static and dynamic scattering media," *Sci. Adv.* **9**, eadg4671 (2023).
29. T. Yeminy and O. Katz, "Guidestar-free image-guided wavefront shaping," *Sci. advances* **7**, eabf5364 (2021).
30. Y. Shen, Y. Chen, Q. Liu, *et al.*, "Improved anscombe transformation and total variation for denoising of lowlight infrared images," *Infrared Phys. & Technol.* **93**, 192–198 (2018).
31. N. Antipa, G. Kuo, R. Heckel, *et al.*, "Diffusercam: lensless single-exposure 3d imaging," *Optica* **5**, 1–9 (2017).

32. X. Deng, C.-I. Tang, C. Luo, and Y. Takashima, “Diffraction efficiency of mems phase light modulator, ti-plm, for quasi-continuous and multi-point beam steering,” *Micromachines* **13**, 966 (2022).
33. B. Chao, M. Gopakumar, S. Choi, and G. Wetzstein, “High-brightness holographic projection,” *Opt. Lett.* **48**, 4041–4044 (2023).
34. S. Choi, M. Gopakumar, Y. Peng, *et al.*, “Time-multiplexed neural holography: a flexible framework for holographic near-eye displays with fast heavily-quantized spatial light modulators,” in *ACM SIGGRAPH 2022 Conference Proceedings*, (2022), pp. 1–9.
35. O. Guyon and J. Males, “Adaptive optics predictive control with empirical orthogonal functions (eof’s),” arXiv preprint arXiv:1707.00570 (2017).
36. C. J. Pellizzari, M. F. Spencer, and C. A. Bouman, “Imaging through distributed-volume aberrations using single-shot digital holography,” *J. Opt. Soc. Am. A* **36**, A20–A33 (2019).
37. K. Yanny, K. Monakhova, R. W. Shuai, and L. Waller, “Deep learning for fast spatially varying deconvolution,” *Optica* **9**, 96–99 (2022).
38. A. Shajkofci and M. Liebling, “Spatially-variant cnn-based point spread function estimation for blind deconvolution and depth estimation in optical microscopy,” *IEEE Trans. on Image Process.* **29**, 5848–5861 (2020).
39. L. Huang, R. Luo, X. Liu, and X. Hao, “Spectral imaging with deep learning,” *Light. Sci. & Appl.* **11**, 61 (2022).
40. E. Edrei and G. Scacelli, “Memory-effect based deconvolution microscopy for super-resolution imaging through scattering media,” *Sci. reports* **6**, 33558 (2016).
41. A. S. Bandeira, J. Cahill, D. G. Mixon, and A. A. Nelson, “Saving phase: Injectivity and stability for phase retrieval,” *Appl. Comput. Harmon. Anal.* **37**, 106–125 (2014).

## Supplementary Information

### Contents

- Section I: Experimental setup and implementation
- Section II: Poisson blind deconvolution algorithm
- Section III: Optical correction for photon-limited imaging
- Section IV: Loss landscape

## I. EXPERIMENTAL SETUP AND IMPLEMENTATION

### A. Optical setup

Figure S1 illustrates the 4f relay optical setup for Turbulence-Aware Poisson blind deconvolution (TAP-BD). The system uses an incoherent LED (M530L4, Thorlabs, CW: 530 nm, FWHM: 35 nm), which passes through a neutral density (ND) filter to simulate low-photon conditions. A narrow bandpass filter (NBP; FLH5532-4, Thorlabs, CW: 532 nm, FWHM: 4 nm) further isolates the desired spectral component. A polarizer ensures that only horizontally polarized light enters the system, aligning with working polarization of the spatial light modulator (SLM).

The light is then focused by lenses L0 and L1 to illuminate the target, with the LED image projected onto the target surface, ensuring the light remains incoherent. The relay system, consisting of lenses L2 and L3, forms an intermediate image after L3. At this stage, Iris1 is introduced for spatial filtering, allowing selective imaging of specific target regions.

Lens L4 performs a Fourier transform of the target image, directing it onto the SLM (E19x12-400-800-HDM8, Meadowlark Optics; 1920×1200 pixels, 8  $\mu\text{m}$  pixel pitch). The SLM applies phase modulation composed of three components: a grating phase, turbulence phase, and multiple phase diversity patterns, as described in subsection IB.

The modulated light is then focused by L5, and Iris2 removes unmodulated zero-order diffraction components. The first-order diffraction patterns (with an efficiency of approximately 0.7–0.8) are captured by the EM-CCD (PiMax4: 512EM, Princeton Instruments; 512×512 pixels, 24  $\mu\text{m}$  pixel pitch). The magnification is determined by the focal length ratio of L5 to L2. In the configurations used, L5 has a focal length of 20 cm (for Fig. 3 in the main text) or 30 cm (for Fig. 4), while L2 has a focal length of 15 cm, resulting in magnifications of 1.3× or 2.0×, respectively. All imaging was performed in a darkroom to minimize background light.

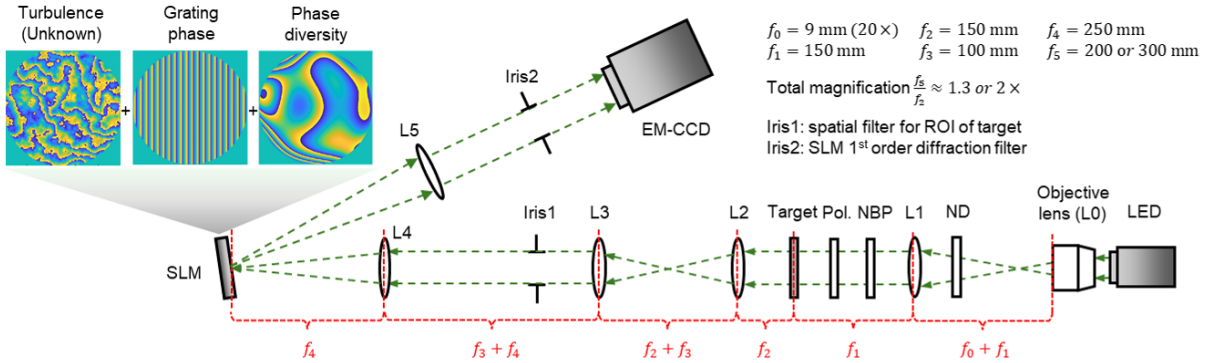


FIG. S1. 4f relay setup with LED illumination and spectral/polarization filtering. incoherent target image is relayed via L2–L5 onto an EM-CCD. A composite phase at the SLM—combining grating, turbulence, and diversity—modulates efield at the Fourier plane. Iris1 selects the region of interest, while Iris2 isolates the 1st-order diffraction.

### B. SLM phase patterns generation

The  $i$ -th SLM phase,  $\Phi_{\text{SLM},i}$  (for  $i = 1, \dots, M$ ), consists of three components:

$$\Phi_{\text{SLM},i} = \Phi_{\text{Grating}} + \Gamma_i + \Phi_{\text{Turbulence}}, \quad (\text{S1})$$

where each component is defined as follows:

1. Grating phase ( $\Phi_{\text{Grating}}$ ): The grating phase  $\Phi_{\text{Grating}}$  spatially separates the 1st-order diffraction patterns from the 0th-order. The blazed grating period  $\Lambda$  is given by:

$$\Lambda = \frac{\lambda \cdot f_5}{d_{\text{shift}} \cdot p_{\text{slm}}}, \quad (\text{S2})$$

where  $\lambda$  is the wavelength,  $f_5$  is the focal length of the imaging lens L5,  $d_{\text{shift}}$  is the lateral shift required to isolate the 1st-order from the 0th-order signal, and  $p_{\text{slm}}$  is SLM pixel size. For our setup,  $\Lambda$  was approximately 3 SLM pixels, corresponding to a lateral shift of about 6 mm when  $f_5 = 30$  cm.

2. Phase diversity ( $\Gamma_i$ ): Phase diversity pattern  $\Gamma_i$  is introduced using the first 15 Zernike polynomials:

$$\Gamma_i = \sum_{n=1}^{15} w_{n,i} Z_n, \quad (\text{S3})$$

where  $\{Z_n\}$  are the Zernike polynomials, and  $\{w_{n,i}\}$  are  $i$ -th Gaussian-distributed random weights with zero mean and variance 20. A total of  $M$  such phase diversity patterns are generated, scaled to the aperture size  $D$ , and zero padded to match the SLM array size.

3. Turbulence Phase ( $\Phi_{\text{Turbulence}}$ ): The turbulence phase  $\Phi_{\text{Turbulence}}$  is the retrieval target. The method for generating  $\Phi_{\text{Turbulence}}$  is detailed in the Appendix or the main text. We refer to  $\Phi_{\text{Turbulence}}$  as  $\Phi$  in subsequent discussions.

To ensure that only the signal inside the aperture contributes to the 1st-order diffraction, the phase outside the aperture with diameter  $D$  is set to zero. This design effectively makes the SLM function as an aperture, preventing unmodulated components from affecting the measurement.

### C. Sample preparation

Three type of samples are used in this work: (1) Negative 1951 USAF target (Thorlab; R3L3S1N), (2) Laser-printed transparent film featuring the Purdue logo, printed at 1200 dpi resolution ( $\sim 0.0212$  mm dot spacing), (3) Beam projector coupled with a  $20 \times$  objective lens to display the Cameraman image. Sample (1) and (2) are located at target location in Fig S1, while sample (3) is placed at L3 in the same figure.

## II. POISSON BLIND DECONVOLUTION ALGORITHM

The TAP-BD framework is designed to jointly reconstruct the target  $O$ , the set of PSFs  $\{h_i\}$ , and the turbulence phase  $\Phi$ , ensuring robust image recovery under challenging low-photon conditions. To achieve this, PBD employs a three-step approach:

1. Poisson denoising: A plug-and-play (PnP) Poisson denoiser is applied to preprocess noisy measurement, mitigating the effects of Poisson shot noise.
2. blind deconvolution (BD): The target  $O$  and the set of PSFs  $\{h_i\}$  are iteratively estimated by enforcing a global consistency constraint on  $O$  across the multiple denoised measurements. BD module is introduced to model the image formation physics, specifically the convolutional relationship between the object and the PSF.
3. turbulence phase retrieval (PR): The turbulence phase  $\Phi$  is refined using the reconstructed PSFs  $\{h_i\}$  from the BD stage and phase diversity patterns  $\Gamma_i$ . This step accounts for wave propagation physics in the PSF. The reconstructed  $\Phi$  is then reintroduced into BD as the updated PSFs model, iteratively refining both the target  $O$  and turbulence phase  $\Phi$ .

Steps (2) and (3) are integrated into each iteration, ensuring a joint optimization process that continuously updates both the object reconstruction and turbulence estimation. The overall workflow is illustrated in Figure S2.

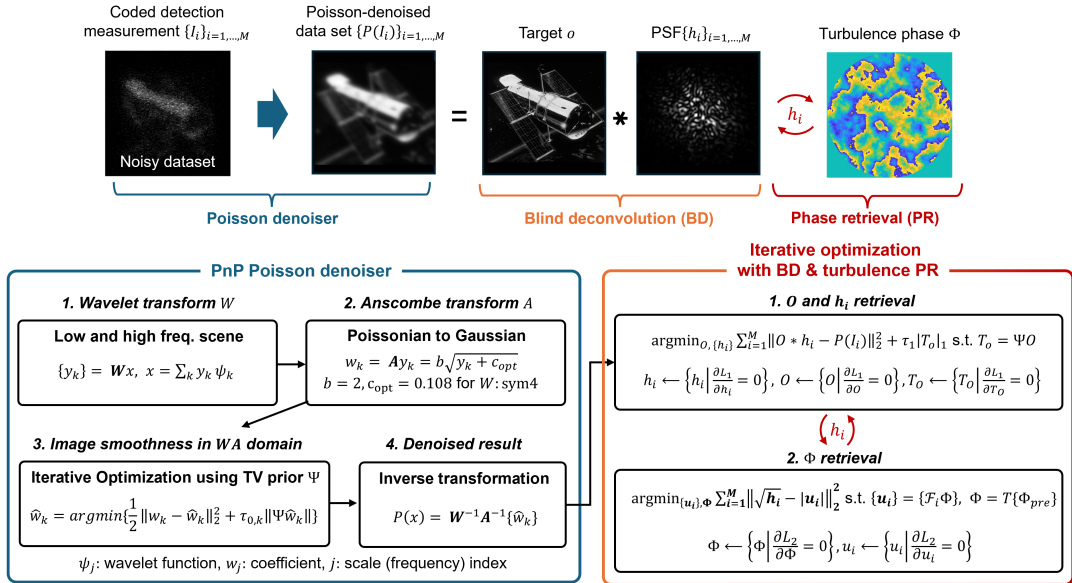


FIG. S2. Overview of the Turbulence-Aware Poisson Blind Deconvolution (TAP-BD) framework. The process begins with PnP Poisson denoising, transforming noisy measurements into a denoised dataset. This is followed by blind deconvolution (BD), which reconstructs the target  $O$  and the set of PSFs  $\{h_i\}$ . Turbulence phase retrieval (PR) then refines the turbulence phase  $\Phi$  using the intermediate PSFs  $\{h_i\}$  estimated in the BD stage. BD and PR are iteratively optimized, leveraging the denoised inputs to achieve robust reconstruction under low-photon conditions.

### A. Poisson denoiser

To stabilize reconstruction under severe shot noise, TAP-BD applies a Poisson denoiser in the PnP step, transforming noisy inputs  $\{I_i\}$  into denoised data  $\{P_i\}$ , following [1]. This step reduces noise across photon levels and complements Gaussian-optimized TV regularization without requiring extensive tuning.

The denoiser first applies wavelet decomposition  $\mathbf{W}$  to the raw Poissonian measurement  $x$ , separating it into frequency bands:

$$\{y_k\}_{k=1,\dots,K} = \mathbf{W}x, \quad x = \sum_k y_k \psi_k, \quad (S4)$$

where  $\psi_k$  is the wavelet function (here, sym4),  $\{y_k\}$  are the 2D wavelet coefficients, and  $k$  indexes frequency bands. Only the first (LL) and last (HH) frequency components are used.

Next, the wavelet-based data undergoes the Anscombe transform  $\mathbf{A}$  to map the Poissonian measurements to the Gaussian domain for improved noise handling:

$$w_k = \mathbf{A}y_k = b\sqrt{y_k + c_{opt}}, \quad (S5)$$

Where  $b = 2$  and  $c_{opt} = 0.108$  are fixed parameters for sym4, following [1].

The transformed wavelet coefficient  $\{w_k\}$  are then smoothed using TV regularization to remove noise effect while preserving essential details:

$$\hat{w}_k = \text{argmin} \frac{1}{2} \|w_k - \hat{w}_k\|_2^2 + \tau_{0,k} \|\Psi\hat{w}_k\|, \quad (S6)$$

where  $\Psi$  is the TV operator and  $\tau_{0,k}$  controls smoothness based on mean photons level.

Finally, the inverse Anscombe and wavelet transforms restore the denoised data:

$$P(x) = \mathbf{W}^{-1}\mathbf{A}^{-1}\{\hat{w}_k\}, \quad (S7)$$

This step stabilizes reconstruction across photon levels by reducing sensitivity to hyperparameter settings (Fig. S3). At high photon counts, however, the denoiser may slightly degrade image quality [1].

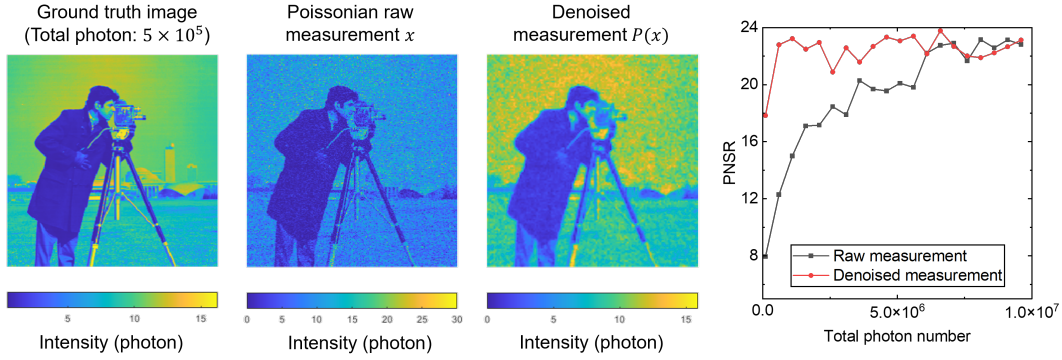


FIG. S3. Poisson denoiser effectively reduces shot noise in the low-photon regime, significantly improving PSNR and preserving key image features.

### B. Blind deconvolution (BD)

In the BD framework, the optimization problem seeks to jointly estimate the target  $O$  and a set of PSFs  $\{h_i\}$  from the denoised measurements  $\{P_i\}$ . The reconstruction of the single target  $O$  acts as a consistency constraint across measurements  $\{P_i\}$ , improving PSFs estimation by ensuring they align with the same target  $O$ . In the BD framework, the objective function is:

$$\underset{O, \{h_i\}_{i=1, \dots, M}}{\operatorname{argmin}} \sum_{i=1}^M \left[ \frac{1}{2} \|h_i * O - P_i\|^2 \right] + \tau_1 \|T_O\|, \quad \text{s.t. } T_O = \Psi O, \quad (\text{S8})$$

where  $P_i = P(I_i)$  represents the denoised measurements from the Poisson denoiser on the observed data  $I_i$ . Here,  $T_O$  is an auxiliary variable subject to TV regularization, and  $\Psi$  is the TV operator. The operator  $\Psi O$  produces two images representing vertical and horizontal differences, expressed as:

$$\Psi O_{i,j} = \begin{bmatrix} O_{i+1,j} - O_{i,j} \\ O_{i,j+1} - O_{i,j} \end{bmatrix}. \quad (\text{S9})$$

Using the augmented Lagrangian approach, we transform this constrained optimization problem into an unconstrained form:

$$L_1(O, T_O, \{h_i\}_{i=1, \dots, M}, \lambda_1) = \sum_{i=1}^M \left[ \frac{1}{2} \|h_i * O - P_i\|^2 \right] + \tau_1 \|T_O\| + \frac{\gamma_1}{2} \|T_O - \Psi O + \lambda_1\|^2, \quad (\text{S10})$$

where  $\lambda_1$  is a dual variable (Lagrange multiplier), and  $\gamma_1$  is the penalty parameter.

To solve for  $O$ ,  $T_O$ ,  $\{h_i\}$ , and  $\lambda_1$ , we apply the alternating direction method of multipliers (ADMM), which optimizes each variable sequentially while holding the others fixed. This iterative process updates each variable at the  $j$ -th iteration as follows:

$$O^{(j+1)} = \underset{O}{\operatorname{argmin}} L_1(O, T_O^{(j)}, \{h_i^{(j)}\}_{i=1, \dots, M}, \lambda_1^{(j)}) \quad (\text{S11})$$

$$T_O^{(j+1)} = \underset{T_O}{\operatorname{argmin}} L_1(O^{(j+1)}, T_O, \{h_i^{(j)}\}_{i=1, \dots, M}, \lambda_1^{(j)}) \quad (\text{S12})$$

$$\{h_i^{(j+1)}\}_{i=1, \dots, M} = \underset{\{h_i\}_{i=1, \dots, M}}{\operatorname{argmin}} L_1(O^{(j+1)}, T_O^{(j+1)}, \{h_i\}, \lambda_1^{(j)}) \quad (\text{S13})$$

$$\lambda_1^{(j+1)} = \lambda_1^{(j)} + \gamma_1 (T_O^{(j+1)} - \Psi O^{(j+1)}). \quad (\text{S14})$$

Here,  $\lambda_1$  is updated through a gradient ascent step, gradually enforcing constraint satisfaction in the augmented Lagrangian. While methods like stochastic gradient descent could be used, we employ closed-form solutions using stationary points to accelerate convergence. For analytical gradient calculation, we have to express each operation as

pointwise (or matrix multiplication in a diagonal form) in a specific basis. In the Fourier domain, the convolution term  $h_i * O$  simplifies to pointwise multiplication, expressed as:

$$\mathcal{F}\{h_i * O\} = \mathcal{F}\{h_i\} \cdot \mathcal{F}\{O\} \implies h_i * O = \mathcal{F}^{-1}\{\mathcal{F}\{h_i\} \cdot \mathcal{F}\{O\}\}. \quad (\text{S15})$$

To simplify gradients  $\frac{\partial L_1}{\partial O}$  and  $\frac{\partial L_1}{\partial h_i}$ , we shift to the Fourier domain, where convolutions become multiplications. Defining Fourier-transformed variables, e.g.,  $\tilde{x} = \mathcal{F}(x)$ , we rewrite  $L_1$  as:

$$L_1(\tilde{O}, \tilde{T}_O, \{\tilde{h}_i\}_{i=1,\dots,M}, \tilde{\lambda}_1) = \sum_{i=1}^M \left[ \frac{1}{2} \|\tilde{h}_i \tilde{O} - \tilde{P}_i\|^2 \right] + \tau_1 \|\tilde{T}_O\| + \frac{\gamma_1}{2} \|\tilde{T}_O - \tilde{\Psi} \tilde{O} + \tilde{\lambda}_1\|^2. \quad (\text{S16})$$

Setting  $\frac{\partial L_1}{\partial \tilde{O}} = 0$ , we obtain:

$$\frac{\partial L_1}{\partial \tilde{O}} = \sum_{i=1}^M \left[ (\tilde{h}_i^j)^H (\tilde{h}_i^j \tilde{O} - \tilde{P}_i) \right] - \gamma_1 \tilde{\Psi}^H (\tilde{T}_O^j - \tilde{\Psi} \tilde{O} + \tilde{\lambda}_1^j) = 0, \quad (\text{S17})$$

where  $(\tilde{h}_i^j)^H$  and  $\tilde{\Psi}^H$  are the Hermitian adjoint operators in the Fourier domain.

Rearranging this expression, the update rule for  $\tilde{O}$  is:

$$\tilde{O}^{(j+1)} = \left( \sum_{i=1}^M (\tilde{h}_i^j)^H \tilde{h}_i^j + \gamma_1 \tilde{\Psi}^H \tilde{\Psi} \right)^{-1} \left( \sum_{i=1}^M (\tilde{h}_i^j)^H \tilde{P}_i - \gamma_1 \tilde{\Psi}^H (\tilde{T}_O^j + \tilde{\lambda}_1^j) \right). \quad (\text{S18})$$

Applying the inverse Fourier transform, we recover:

$$O^{(j+1)} = \text{Re}(\mathcal{F}^{-1}(\tilde{O}^{(j+1)})). \quad (\text{S19})$$

The operation  $\tilde{\Psi}^H x = \mathcal{F}[\Psi^H x]$  represents the Fourier transform of the adjoint TV operator  $\Psi^H$ , which sums horizontal and vertical pixel differences. Specifically,  $\Psi^H O_{i,j}$  is given by:

$$\Psi^H O_{i,j} = (O_{i-1,j}^y - O_{i,j}^y) + (O_{i,j-1}^x - O_{i,j}^x). \quad (\text{S20})$$

To efficiently compute  $\tilde{\Psi}^H \tilde{\Psi}$  in the Fourier domain, one can define a Laplacian-like filter centered on the main pixel with offsets for adjacent pixels as:

$$\Psi^H \Psi = \begin{cases} 4, & \text{at } (0, 0), \\ -1, & \text{at } (1, 0), (-1, 0), (0, 1), (0, -1), \\ 0, & \text{otherwise.} \end{cases} \quad (\text{S21})$$

Then,  $\tilde{\Psi}^H \tilde{\Psi} = |\mathcal{F}[\Psi^H \Psi]|$ . Further details on implementing  $\Psi$  in ADMM are available at [2, 3].

For  $T_O$ , we optimize directly in the spatial domain, as it does not involve convolution terms. Setting  $\frac{\partial L_1}{\partial T_O} = 0$ , we derive the following update rule:

$$\frac{\partial L_1}{\partial T_O} = \tau_1 \text{sign}(T_O) + \gamma_1 (T_O - \Psi O^{(j+1)} + \lambda_1^{(j)}) = 0. \quad (\text{S22})$$

This simplifies to:

$$T_O^{(j+1)} = \text{sign}(\Psi O - \lambda_1) \max \left( 0, |\Psi O - \lambda_1| - \frac{\tau_1}{\gamma_1} \right). \quad (\text{S23})$$

Next, finding stationary points for  $h_i$  using a closed-form optimization yields a Wiener deconvolution-like update rule with  $\gamma_2$  as a stabilization term, similar to the noise power spectral density (PSD) in Wiener deconvolution:

$$\tilde{h}_i^{(j+1)} = \left( \sum_{i=1}^M (\tilde{O}^{(j+1)})^H \tilde{O}^{(j+1)} + \gamma_2 \right)^{-1} \left( \sum_{i=1}^M (\tilde{O}^{(j+1)})^H \tilde{P}_i \right) \quad (\text{S24})$$

Similar to the  $O$  update, by applying the inverse Fourier transform, we recover:

$$h_i^{(j+1)} = \text{Re}(\mathcal{F}^{-1}(\tilde{h}_i^{(j+1)})). \quad (\text{S25})$$

Note that the denoising capability can be adjusted using  $\gamma_2$ , but even a small amount of residual noise can significantly impact the subsequent phase retrieval updates. To address this more effectively, we introduced a PnP soft thresholding on  $h_i$  to suppress residual noise, followed by the  $h_i$  update rule. This PnP thresholding is applied as:

$$\hat{h}_i^{(j+1)} = \text{sign}(h_i^{(j+1)}) \max \left( 0, |h_i^{(j+1)}| - \tau_2 \right). \quad (\text{S26})$$

Also, if necessary, one can use additional constraint on  $h_i$  to prevent the tendency of  $h_i$  to go too far outward by additionally applying aperture constraint. This step further stabilizes the PSF estimation, resulting in potential improvement of reconstruction performance in turbulence phase retrieval (PR).

### C. Phase retrieval (PR)

In this PR module, we incorporate two main inputs: (1) An intermediate set of estimates  $\{\hat{h}_i\}$  from the previous BD module, (2) corresponding set of phase diversity patterns  $\{\Gamma_i\}$ .

The objective function of the PR framework is to reconstruct the complex e-field  $\Phi$  by solving:

$$\underset{\{u_i\}_{i=1,\dots,M}, \Phi}{\text{argmin}} \sum_{i=1}^M \frac{1}{2} \left\| \sqrt{\hat{h}_i} - |u_i| \right\|^2, \quad \text{s.t. } u_i = \mathcal{F}_i \Phi, \quad (\text{S27})$$

where  $u_i$  is an auxiliary PSF e-field at the image plane, and  $\mathcal{F}_i$  incorporates wave propagation with the  $i$ -th phase diversity pattern  $\Gamma_i$ . Using the augmented Lagrangian method, the constrained optimization problem is reformulated as:

$$L_2(\{u_i\}_{i=1,\dots,M}, \Phi) = \sum_{i=1}^M \frac{1}{2} \left\| \sqrt{\hat{h}_i} - |u_i| \right\|^2 + \frac{\gamma_3}{2} \|u_i - \mathcal{F}_i \Phi + \lambda_3\|^2 \quad (\text{S28})$$

One might notice that the angle of  $u_i$  is solely given by the second term, so:

$$\angle u_i = \angle(\mathcal{F}_i \Phi - \lambda_3). \quad (\text{S29})$$

To solve for  $|u_i|$ , we derive the stationary point of  $L_2$  with respect to  $|u_i|$  as:

$$\frac{\partial L_2}{\partial |u_i|} = - \left( \sqrt{\hat{h}_i} - |u_i| \right) + \gamma_3 (|u_i| - |\mathcal{F}_i \Phi - \lambda_3|) = 0. \quad (\text{S30})$$

Leading to the update:

$$|u_i^{(j+1)}| = (1 + \gamma_3)^{-1} \left( \sqrt{\hat{h}_i^{(j+1)}} + \gamma_3 |\mathcal{F}_i \Phi^{(j)} - \lambda_3^{(j)}| \right) \quad (\text{S31})$$

Thus, the entire  $u_i$  is updated as:

$$u_i^{(j+1)} = (1 + \gamma_3)^{-1} \left( \sqrt{\hat{h}_i^{(j+1)}} + \gamma_3 |\mathcal{F}_i \Phi^{(j)} - \lambda_3^{(j)}| \right) \exp \left( j \angle \left( \mathcal{F}_i \Phi^{(j)} - \lambda_3^{(j)} \right) \right) \quad (\text{S32})$$

For a complex variable  $\Phi$ , we solve:

$$\frac{\partial L_2}{\partial \Phi} = \sum_{i=1}^M -\gamma_3 \mathcal{F}_i^H (u_i - \mathcal{F}_i \Phi + \lambda_3) = 0 \quad (\text{S33})$$

resulting in the closed-form update:

$$\Phi^{(j+1)} = \left( \sum_{i=1}^M \gamma_3 \mathcal{F}_i^H \mathcal{F}_i \right)^{-1} \left( \sum_{i=1}^M \gamma_3 \mathcal{F}_i^H (u_i^{(j+1)} + \lambda_3^{(j)}) \right) \quad (\text{S34})$$

Here,  $\mathcal{F}_i^H$  is the backpropagation operator, and  $\mathcal{F}_i^H \mathcal{F}_i = 1$ . The dual variable is updated via gradient ascent as:

$$\lambda_3^{(j+1)} = \lambda_3^{(j)} + \gamma_3 \left( u_i^{(j+1)} - \mathcal{F}_i \Phi^{(j+1)} \right) \quad (\text{S35})$$

$$(\text{S36})$$

By refining  $\Phi$  based on multiple intermediate PSF estimates and feeding it back to the BD as:

$$h_i^{(j+1)} = |\mathcal{F}_i \Phi^{(j+1)}|^2 \quad (\text{S37})$$

This alternating BD-PR update framework enables robust parameter estimation by integrating two distinct image formation models: incoherent convolution for the target and PSF recovery, and coherent wave propagation for turbulence phase retrieval. The pseudocode below outlines the PBD algorithm's iterative steps.

---

**Algorithm 1** Pseudocode for PBD algorithm

---

<b>Input:</b>	Multiple noisy measurements $\{I_i\}_{i=1,\dots,M}$ , and corresponding phase diversity patterns $\{\Gamma_i\}_{i=1,\dots,M}$ , hyperparameters $\tau_0 = [1 + 1/\bar{\mu}, 4 + 1/\bar{\mu}]$ [1], $\gamma_1 = 1e^{-2}$ , $\tau_1 = 1e^{-5}\gamma_1$ , $\gamma_2 = 5e^{-6}$ , $\tau_2 = 3e^{-2}$ , $\gamma_3 = 1e^{-3}$ , where $\bar{\mu}$ is mean photon per pixel.
<b>Output:</b>	Reconstructed target $O$ , PSFs $\{h_i\}_{i=1,\dots,M}$ , turbulence phase $\Phi$
<b>1. Initialization</b>	Set $O^{(0)}$ , $\{h_i^{(0)}\}$ , $\Phi^{(0)}$ , $\{\lambda_1^{(0)}\}$ , $\lambda_3^{(0)}$ , initialize parameters and max_iter.
<b>2. PnP Poisson Denoising</b>	For each noisy measurement $I_i$ : Apply wavelet decomposition: $\{y_{i,k}\} = \mathbf{W}(I_i)$ Eq. S5 Apply Anscombe transform: $w_{i,k} = \mathbf{A}(y_{i,k})$ Eq. S4 Solve: $\hat{w}_{i,k} = \arg \min_{\hat{w}_{i,k}} \frac{1}{2} \ w_{i,k} - \hat{w}_{i,k}\ ^2 + \tau_0, k \ \Psi w_{i,k}\ $ Eq. S6 Reconstruct denoised data: $P_i = \mathbf{W}^{-1} \mathbf{A}^{-1} \{\hat{w}_{i,k}\}$ Eq. S7
<b>3. Iterative Optimization</b>	For $j = 1, \dots, \text{max\_iter}$ : <b>a. Blind Deconvolution (BD)</b> Update target $O$ : $O^{(j+1)} = \mathcal{F}^{-1} \left( \left( \sum_{i=1}^M (\tilde{h}_i^j)^H \tilde{h}_i^j + \gamma_1 \tilde{\Psi}^H \tilde{\Psi} \right)^{-1} \left( \sum_{i=1}^M (\tilde{h}_i^j)^H \tilde{P}_i - \gamma_1 \tilde{\Psi}^H (\tilde{T}_O^j + \tilde{\lambda}_1^j) \right) \right) \quad \text{Eq. S18, S19}$ Update target smoothness $T_O$ : $T_O^{(j+1)} = \text{sign}(\Psi O - \lambda_1) \max \left( 0,  \Psi O - \lambda_1  - \frac{\tau_1}{\gamma_1} \right) \quad \text{Eq. S23}$ Update $\lambda_1$ : $\lambda_1^{(j+1)} = \lambda_1^{(j)} + \gamma_1 \left( T_O^{(j+1)} - \Psi O^{(j+1)} \right) \quad \text{Eq. S14}$ Update PSFs $\{h_i\}$ : $h_i^{(j+1)} = \mathcal{F}^{-1} \left( \left( \sum_{i=1}^M (\tilde{O}^{(j+1)})^H \tilde{O}^{(j+1)} + \gamma_2 \right)^{-1} \left( \sum_{i=1}^M (\tilde{O}^{(j+1)})^H \tilde{P}_i \right) \right) \quad \text{Eq. S24, S25}$ Apply PnP soft-thresholding on PSFs $\{h_i\}$ : $\hat{h}_i^{(j+1)} = \text{sign}(h_i^{(j+1)}) \max(0,  h_i^{(j+1)}  - \tau_2) \quad \text{Eq. S26}$ <b>b. Phase Retrieval (PR)</b> Update auxiliary field $u_i$ : $u_i^{(j+1)} = (1 + \gamma_3)^{-1} \left( \sqrt{\hat{h}_i^{(j+1)}} + \gamma_3  \mathcal{F}_i \Phi^{(j)} - \lambda_3^{(j)}  \right) \exp \left( j \angle \left( \mathcal{F}_i \Phi^{(j)} - \lambda_3^{(j)} \right) \right) \quad \text{Eq. S32}$ Update turbulence phase $\Phi$ : $\Phi^{(j+1)} = (M \gamma_3)^{-1} \left( \sum_{i=1}^M \gamma_3 \mathcal{F}_i^H (u_i^{(j+1)} + \lambda_3^{(j)}) \right) \quad \text{Eq. S34}$ Update $\lambda_3$ and $\lambda_4$ : $\lambda_3^{(j+1)} = \lambda_3^{(j)} + \gamma_3 \left( u_i^{(j+1)} - \mathcal{F}_i \Phi^{(j+1)} \right) \quad \text{Eq. S35}$ Update PSFs: $h_i^{(j+1)} =  \mathcal{F}_i \Phi^{(j+1)} ^2$ Eq. S37
<b>4. Output</b>	Return $O$ , $\{h_i\}_{i=1,\dots,M}$ , and $\Phi$ .

---

### III. OPTICAL CORRECTION FOR PHOTON-LIMITED IMAGING

Figure 4 in the main text shows that TAP-BD improves reconstruction, especially in low-photon regimes, when using the Poisson denoiser. While phase RMSE gains are modest and less intuitive, we validate their impact by applying the reconstructed phase for turbulence compensation and evaluating optical correction performance.

Figure S4 shows experimental results using a projected cameraman image and a  $20 \times$  lens. Without Poisson denoising (A), TAP-BD fails to recover meaningful details under  $< 1.07 \times 10^7$  photons. With denoising (B), essential phase features are preserved, enabling better optical correction despite only modest RMSE improvement (C, top). PSNR gains are significant—for instance, rising from 12 dB to 20 dB between  $0.32$  and  $2.10 \times 10^7$ . This suggests that the

denoiser helps the reconstructed phase retain critical features not fully captured by phase RMSE alone, underscoring its robustness in photon-starved conditions.

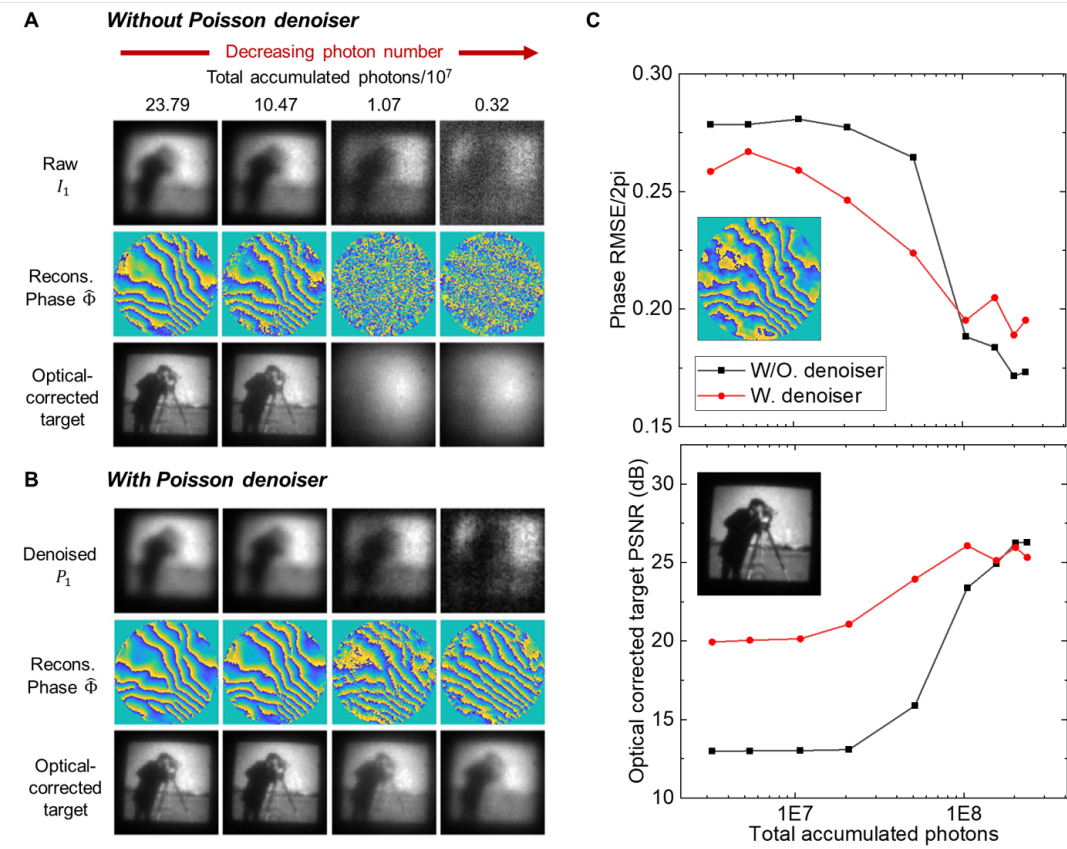


FIG. S4. Comparison of TAP-BD reconstruction with and without Poisson denoising under varying photon levels for a projected cameraman target. (A–B) From top to bottom: raw/denoised measurements, reconstructed phases, and optically corrected targets. The Poisson denoiser preserves key phase features in low-photon regimes, enabling improved correction. (C) Quantitative comparison of phase RMSE and corrected-target PSNR. Insets show ground truth phase and diffraction-limited target. All results use a 6 mm aperture, 48 SLM patterns, and 1000 iterations.

#### IV. LOSS LANDSCAPE

Figures 3 and 4 highlight key factors that boost reconstruction performance. Figure 3 shows that more measurements improve accuracy, while Figure 4 demonstrates the Poisson denoiser’s effectiveness in low-photon conditions. These trends align with intuition: additional measurements offer more information, and denoising mitigates shot noise (see also Figures S3, S4).

To better understand this, we analyzed the loss landscape by perturbing two components of the estimated turbulence phase  $\hat{\Phi}$ , generating PSFs  $\{h_i\}$  (Eq. S37), and evaluating the  $L_1$  loss terms (Eq. S10). Figure S5 shows that increasing measurements steepens and deepens the loss curvature, guiding optimization more effectively.

Figure S6 compares the loss landscape with and without the Poisson denoiser. Without the denoiser, particularly at low photon levels, the loss curvature becomes shallow, and multiple stationary points emerge, making convergence less reliable. In contrast, with the Poisson denoiser, the loss landscape exhibits well-defined minima, improving robustness, and ensuring more stable convergence.

[1] Y. Shen, Y. Chen, Q. Liu, S. Lou, W. Yu, X. Wang, and H. Chen, Improved anscombe transformation and total variation for denoising of lowlight infrared images, *Infrared Physics & Technology* **93**, 192 (2018).

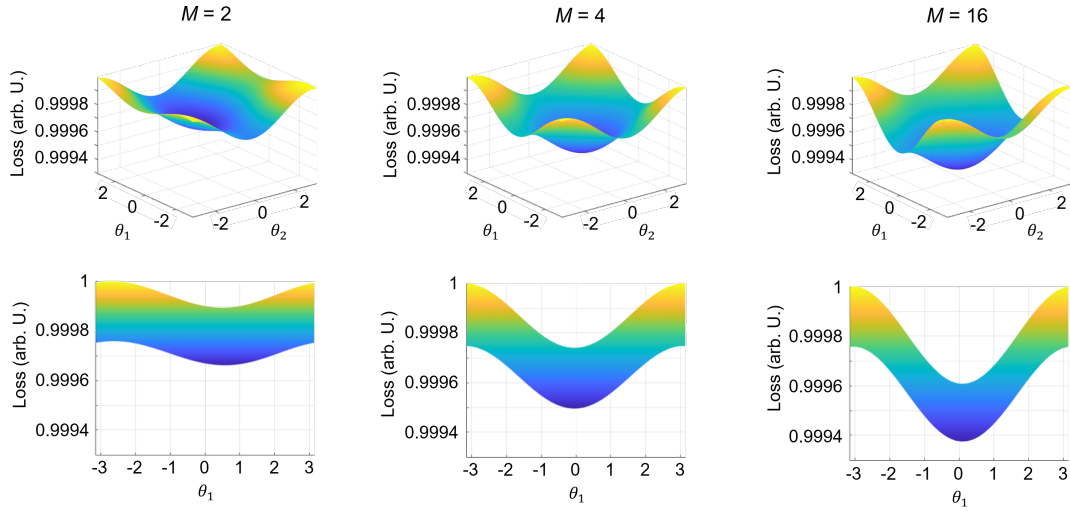


FIG. S5. Loss landscape vs. varying number of measurements. The landscape is derived by perturbing two phase parameters in reconstructed phase  $\hat{\Phi}$ , generating a corresponding set of PSFs  $\{h_i\}_{i=1,\dots,M}$ , which is then applied to the  $L_1$  (eq. S10). Increasing measurements gives deeper and steeper loss curvature, resulting in more precise guidance toward the minima.

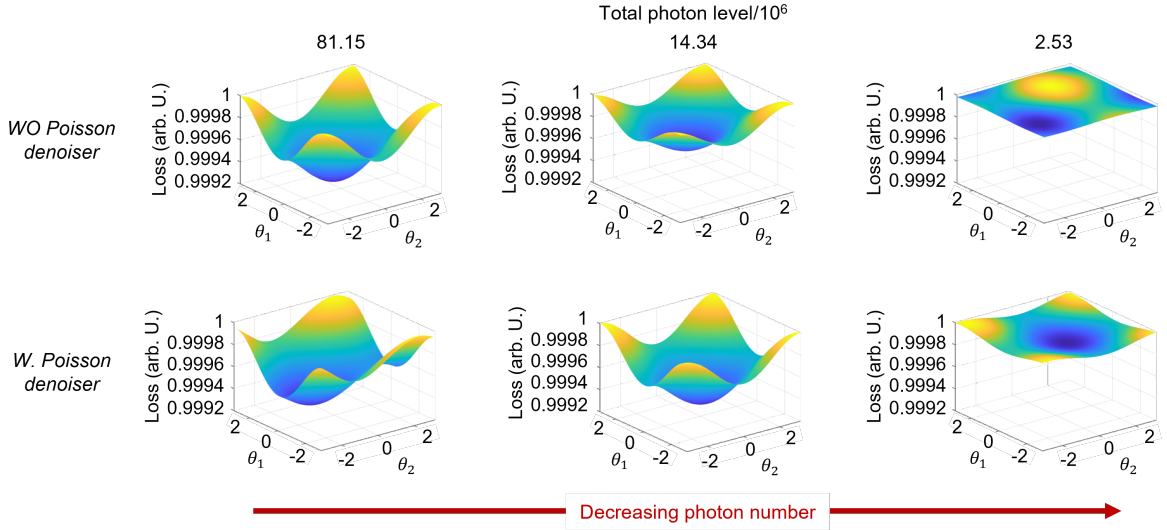


FIG. S6. Loss landscapes with and without the Poisson denoiser for varying photon numbers. The application of the Poisson denoiser stabilizes the loss landscape, providing deeper and well-defined minima, particularly in the low-photon regime ( $14.32 \times 10^6$  and  $2.53 \times 10^6$  total photons). However, in high-photon case ( $81.15 \times 10^6$  total photons), the Poisson denoiser does not necessarily improve the loss landscape, consistent with the observations in Fig. S3 and S4.

[2] N. Antipa, G. Kuo, R. Heckel, B. Mildenhall, E. Bostan, R. Ng, and L. Waller, Diffusercam: lensless single-exposure 3d imaging, *Optica* **5**, 1 (2017).  
[3] N. Antipa, G. Kuo, R. Heckel, B. Mildenhall, E. Bostan, R. Ng, and L. Waller, Diffusercam, <http://www.laurawaller.com/research/diffusercam/> (2017), accessed: 2017-11-17.